RSC Advances

PAPER

View Article Online
View Journal | View Issue

Cite this: *RSC Adv.*, 2017, 7, 45470

Ion exchange-prepared $NaSbSe_2$ nanocrystals: electronic structure and photovoltaic properties of a new solar absorber material

Belete Asefa Aragaw,[ab] Jifeng Sun,[c] David J. Singh [c] and Ming-Way Lee *[a]

We report the calculated electronic structure, syntheses and photovoltaic properties of a new ternary solar absorber material $NaSbSe_2$. $NaSbSe_2$ nanocrystals (NCs) have been prepared from a Na–Sb–S precursor by the solution-based Se^{2-} anion exchange reaction. The Na–Sb–S precursor was grown on a TiO_2 electrode using the successive ionic layer adsorption and reaction (SILAR) method. X-ray diffraction shows that the synthesized $NaSbSe_2$ NCs have the same crystal structure as the $NaSbS_2$ precursor with the diffraction angles significantly down-shifted. Energy-dispersive X-ray spectroscopy confirms the complete anion exchange and formation of the $NaSbSe_2$ phase. First principles calculations show that the ordered $NaSbSe_2$ structure resulting from the ion exchange synthesis is important for the performance. The $NaSbSe_2$ NCs have an average size of ~17 nm and a near-optimal optical band gap E_g of 1.48 eV that is lower than the $NaSbS_2$ precursor. Liquid-junction $NaSbSe_2$ quantum dot-sensitized solar cells (QDSSCs) were fabricated from the synthesized $NaSbSe_2$ NCs for the first time. The best cell, prepared using the Au counter electrode and the polysulfide electrolyte, yielded an efficiency of 2.22%, a short current density of 1.31 mA cm^{-2}, an open-circuit voltage of 0.30 V and a fill factor of 56.4% under the reduced light intensity of 10% sun. The external quantum efficiency (EQE) spectrum covers the spectral range of 300–900 nm with a maximum EQE of 75% at $\lambda = 500$ nm. The near-optimal E_g suggests that $NaSbSe_2$ could be a potential material for solar cells. In addition, the ion exchange method can be extended to the preparation of many new metal selenide-based solar materials from their corresponding sulfides. These materials may show improved characteristics compared to samples with more disorder.

Received 21st June 2017
Accepted 15th September 2017

DOI: 10.1039/c7ra06938c

rsc.li/rsc-advances

1. Introduction

Dye-sensitized solar cells (DSSCs) are emerging as a candidate for the next generation of low-cost alternatives to Si photovoltaic devices. Their benefits include solution processing, ease of fabrication, and low costs. Due to the limitations of dye absorbers on the bandwidth of light harvesting as well as synthesis of new and low-cost dyes, inorganic semiconductor quantum dot solar absorbers have acquired increasing attention. Semiconductor quantum dot-sensitized solar cells (QDSSCs), derived on the same principle of a DSSC, are more promising due to the unique properties of semiconductor quantum dot solar absorbers such as band gap tunability and high extinction coefficient.[1–5] Moreover, the multiple exciton generation effect in a quantum dot could push the Shockley–Queisser theoretical efficiency limit of 31% to 44% for single band gap solar cells.[6]

Ternary semiconductors based on metal chalcogenides have a broader range of electrical and optical properties than either the elementary or binary compounds because of the possibility of varying the constituent elements and their compositions. One of the representative ternary semiconductors – the I–V–VI_2 class, where I = Cu, Ag, or alkali metals; V = Sb, Bi; and VI = S, Se, Te, have been studied for their potential applications in thermoelectrics[7–10] and solar cells.[11–16] Among the various I metals, the Cu-based I–V–VI_2 materials, such as Cu–Bi–S, $CuSbS_2$, have been explored as solar materials.[17–21] The Ag-based materials such as $AgSbS_2$, Ag_3SbS_3, and $AgBiS_2$ have also been reported recently.[11,16,22] In contrast, I–V–VI_2 materials based on alkali metals have been rarely investigated despite their ease of preparation and promising solar cell performance.[23] Alkali metal antimony-based ternary chalcogenides of the type $A^{I}SbX_2^{VI}$ (where A = Na, K, Rb and X = S, Se) had been synthesized by the direct interaction of an alkali metal with antimony and either sulphur or selenium at extremely high temperature.[24–26] The cation sublattice of these compounds is often disordered at high temperature and may order or partially order as temperature is lowered.

Recently a member of the alkali antimony $A^{I}SbX^{VI}{}_2$ group – $NaSbS_2$ – has been demonstrated as a potential solar material, achieving a power conversion efficiency of 3.2% under the

---

[a] Institute of Nanoscience and Department of Physics, National Chung Hsing University, Taichung 402, Taiwan. E-mail: mwl@phys.nchu.edu.tw

[b] Department of Chemistry, Bahir Dar University, P.O. Box 79, Bahir Dar, Ethiopia

[c] Department of Physics and Astronomy, University of Missouri, Columbia, MO 65211-7010, USA

reduced light intensity of 0.1 sun.[23] First-principles calculations indicate that the particular electronic structure, which has hybridization between Sb and S p-states of $NaSbS_2$, could provide screening and defect tolerance for carrier collection, making $NaSbS_2$ a potential solar material.[27] Replacing the S element with the heavier Se element lowers the energy gap E_g from 1.8 ($NaSbS_2$) to 1.6 eV ($NaSbSe_2$), as reported by Bazakutsa *et al.*[24] based on measurements on thin film samples. The reduced E_g would lead to a broader optical absorption band, suggesting that $NaSbSe_2$ would have better light harvesting ability than that of $NaSbS_2$, which is a favorable property for a solar material. In addition, $NaSbSe_2$ has a large absorption coefficient of $\alpha = 10^5$ cm^{-1} at $\lambda = 600$ nm.[24] The broad absorption band and large absorption coefficient suggests that $NaSbSe_2$ could be a potential solar absorber material. Moreover, the three elements contained in $NaSbSe_2$ are earth-abundant, low cost, nontoxic and environmentally friendly. However, there has been no report on solar cells based on $NaSbSe_2$ so far. Thin films of $NaSbSe_2$ had been synthesized by thermal evaporation.[24] Here $NaSbSe_2$ nanocrystals (NCs) were produced by selenide ion exchange from a successive ionic layer adsorption reaction (SILAR)-prepared Na–Sb–S precursor. First principles calculations comparing ordered and disordered cation sublattices show that this synthesis method is important as cation disorder reduces the optical band gap to below the useful range. Liquid-junction quantum dot-sensitized solar cells based on $NaSbSe_2$ are demonstrated for the first time. We investigate the effects of ion exchange time and the number of SILAR cycles on the optical spectra and photovoltaic performance of $NaSbSe_2$. We also investigate the dependence of photovoltaic parameters on the types of counter electrode. The best cell yielded an efficiency of 2.2%, a respectable efficiency for the first report of a new solar material.

2. Experimental

2.1 Materials and methods

Preparation of TiO_2 photoelectrode. Fluorine-doped tin oxide glass (FTO, Pilkington, sheet resistance ~7 $\Omega\ \square^{-1}$) was cut to 1.2 × 2.0 cm^2 pieces, followed by cleaning with acetone, methanol and deionized water consecutively for 5 min each under ultrasonic bath. Three layers of TiO_2 films with different particle sizes and film thicknesses were coated layer-by-layer on the FTO substrate. First, a blocking or compact layer of TiO_2 (~90 nm thick) was made by spin-coating (2000 rpm, 60 seconds) an ethanol solution of 0.2 M titanium tetraisopropoxide (TTIP) and annealing at 190 °C for 5 minutes. Second, an active mesoporous TiO_2 layer (Dyesol 30NR-T, particle size ~30 nm, ~10 μm thick) was coated using the doctor blade technique, followed by heating at 125 °C for 10 minutes. Lastly, a scattering layer of TiO_2 (Dyesol WER4-0, particle size ~300 nm, ~5 μm thick) was coated on top of the mesoporous TiO_2 layer.

2.2 Synthesis of $NaSbSe_2$ and device fabrication

The Na–Sb–S precursor was directly grown on a TiO_2 electrode with a single-stage SILAR process. The SILAR growth involved the following steps: first, the TiO_2 electrode was dipped into a 0.1 M $SbCl_3$ solution in ethanol for 15 s for Sb^{3+} ionic layer adsorption, followed by rinsing with pure ethanol and drying in air. Second, this electrode was dipped in to a 0.1 M Na_2S solution in methanol for 1 min, followed by rinsing with pure methanol and drying in air. These two steps together are termed as one SILAR cycle. This process was repeated 11 times to grow 11 SILAR cycles of Na–Sb–S precursor. Meanwhile, a Se^{2-} solution was made by dissolving 0.36 g of selenium powder and 0.3 g of $NaBH_4$ in 125 ml of ethanol under N_2 gas flow. The solution turned from black to colorless within a few minutes, showing the reduction of Se powder to Se^{2-} ion. The Na–Sb–S precursor grown on the TiO_2 electrode was dipped into this solution for the exchange of S^{2-} in the Na–Sb–S structure by Se^{2-} from the solution. Then $NaSbSe_2$ nanocrystals (NCs) were obtained after annealing the material at 300 °C for 40 min under flowing N_2 gas. The $NaSbSe_2$ NCs were further coated with a ZnSe passivation layer to passivate surface defects according to the procedure described in the literature.[28] The solar cells were fabricated by arranging the photoelectrode and counter electrode in a sandwich-type assembly and sealing them with a 190 μm-thick parafilm thermoplastic spacer. Pt and Au-coated FTO substrates were employed as the counter electrodes (CE). Pt CEs were made by dropping a 0.005 M H_2PtCl_6 ethanol solution on an FTO substrate, followed by annealing in a furnace at 400 °C for 15 min. This is below the temperature of ~480 °C at which cation disorder is induced.[24] The Au CE film, ~70 nm in thickness, was deposited onto an FTO substrate by sputtering. The polysulfide electrolyte consisted of 0.25 M Na_2S, 1 M S, 0.2 M KCl, and 0.1 M KI in a methanol/DI water (volume ratio 7 : 3) solution. The electrolyte was injected separately through a predrilled hole on the counter electrode into the cell.

2.3 Material characterization and photovoltaic measurements

The crystalline structure and phase purity of $NaSbSe_2$ was analyzed by X-ray diffraction (XRD, Bruker, D8 SSS). Transmission electron microscope (TEM, Joel JEM-2010) was used to determine the crystal size and morphology. Optical property was studied using a Hitachi U-2800A UV-Vis spectrophotometer. The complete ion exchange and elemental analysis was confirmed by energy-dispersive X-ray spectroscopy (EDS coupled SEM, JEOL, JSM-7600F). The photovoltaic performance was studied by measuring photocurrent–voltage (*I*–*V*) curves using a Keithley 2400 source meter under 100 mW cm^{-2} light illumination from an Oriel 150 W Xe lamp with an Oriel bandpass filter simulating the AM 1.5 solar spectrum. External quantum efficiency (EQE) was measured using the monochromatic light generated from a 250W tungsten halogen lamp.

2.4 First principles calculations

Two structural models were investigated. The first was a monoclinic structure based on the structure of $NaSbS_2$, with S replaced by Se and fully relaxed lattice parameters and atomic positions. This model represents the experimental samples studied here. The second model is a model is a special quasirandom structure (SQS) with cation disorder. We used the reported NaCl structure lattice parameter of 5.966 Å and constructed a 16 atom supercell following the method of Wei and Zunger.[29] The atomic coordinates were fully relaxed. The structure relaxations were done using the generalized gradient approximation (GGA) of Perdew, Burke and Ernzerhof (PBE).[30] The full relaxation for the monoclinic structure was done using the projector augmented wave (PAW) method as implemented in the VASP code,[31] with a cut-off energy of 400 eV. All other calculations were done using the linearized augmented plane-wave (LAPW) method as implemented in the WIEN2k code. Electronic structures and optical properties were obtained using the modified Becke–Johnson (mBJ) potential, which generally give improved band gaps compared to the PBE GGA.[32,33] LAPW spheres of radius 2.3 Bohr were used for all atoms, and spin–orbit was included.

3. Results and discussion

The Na–Sb–S precursor was synthesized based on the reaction between Sb_2S_3 and Na_2S as given in eqn (1) below,[34]

$$Sb_2S_3 + Na_2S \rightarrow 2NaSbS_2. \tag{1}$$

After annealing the Na–Sb–S precursor under N_2 gas, clear diffraction peaks, shown in Fig. 1 (middle panel), appearing at 16.81, 21.51, 28.60, 30.59, 31.56, 35.40, 43.83, and 45.31° all match well with the (110), (020), ($\bar{1}12$), ($\bar{2}21$), (002), ($\bar{1}31$), (221) and ($\bar{2}23$) planes of the monoclinic $NaSbS_2$ reference pattern (JCPDS No. 00-032-1039). There are no other impurity phases observed in the spectrum. The other larger peaks observed belong to either TiO_2 or the FTO substrate (labeled as # in the figure).

The pre-annealed $NaSbS_2$ precursor was used for S^{2-} exchange with Se^{2-}, as demonstrated by eqn (2),

$$NaSbS_2 + Se^{2-} \rightarrow NaSbSe_2 + S^{2-} \tag{2}$$

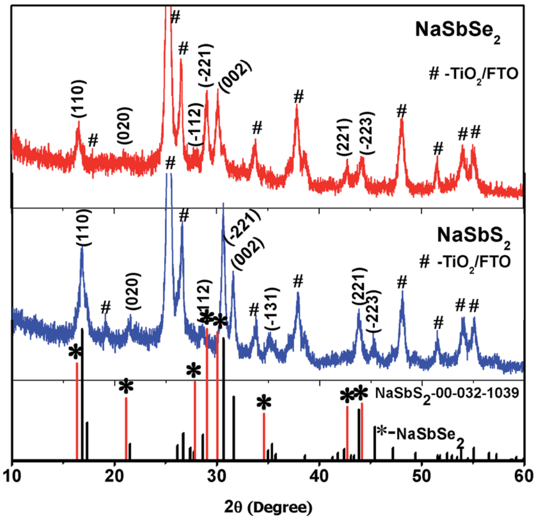

Fig. 1 X-ray diffraction patterns of $NaSbSe_2$ and $NaSbS_2$ nanocrystals. Bottom panel: black lines: $NaSbS_2$ reference pattern; red lines with * symbol: $NaSbSe_2$ reference pattern.

The basis of eqn (2) is explained as follows. The most important factor for driving the ion exchange reaction is the thermodynamic factor. Ions in a solid with a relatively higher solubility can be exchanged by other ions in solution if the product has a lower solubility. The solubility product (K_{sp}), is related to the free energy change of the process. The K_{sp} of metal selenides is lower than that of metal sulfide. Even though the actual solubility can be controlled by many factors, the solubility products of metal chalcogenides have a lower value as the ionic radius of chalcogen increases. That is the ion exchange of S in the crystal with Se^{2-} is thermodynamically feasible process. Once the ion exchange is initiated on the solid–solution interface, further exchange requires the diffusion of ions towards the core of the solid. The inward selenium ion diffusion is accompanied with sulfur ion diffuse towards the solution. In addition, the time required for the exchange reaction is a function of the magnitude of the kinetic barrier for the process.

X-ray diffraction analysis of $NaSbSe_2$ confirms the successful preparation of single-phase $NaSbSe_2$ NCs (Fig. 2, top panel). The pronounced $NaSbSe_2$ peaks are (110), ($\bar{2}21$), (002), (221), and ($\bar{2}23$). After conversion to $NaSbSe_2$, the crystal structure maintained the same monoclinic phase with each (*hkl*) peak shifted to a lower angle relative to the corresponding $NaSbS_2$ peak. For example, the (002) plane shifted from 31.53 ($NaSbS_2$) to 30.13 ($NaSbSe_2$). Our first principles calculations yield lattice parameters, $a = 8.433$ Å, $b = 7.230$ Å, $c = 8.716$ Å, $\gamma = 59.986°$, for a volume 16% larger (~5% linear expansion) than the sulfide, in reasonable accord with these shifts in diffraction peak position. The lower angle shifts are due to lattice expansion as a result of the replacement of smaller S^{2-} (0.184 nm) with larger Se^{2-} (0.198 nm). A size difference of 0.014 nm per atom produces a significant lattice expansion after a complete exchange of S^{2-} with Se^{2-}, which is in agreement with the significant lower angle shifts of the $NaSbSe_2$ peaks relative to the $NaSbS_2$ peaks. The monoclinic structure found is to be contrasted with that normally obtained by high temperature synthesis, which is NaCl with cation disorder, and partial ordering below 480 °C. The average crystallite size of the $NaSbSe_2$ NCs, calculated using the Scherrer's equation from the dominant diffraction peak, is

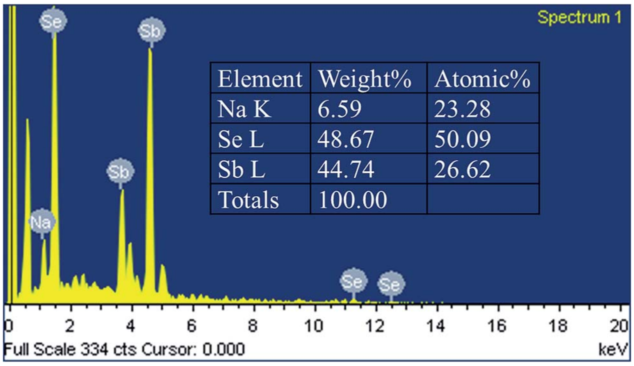

Element	Weight%	Atomic%
Na K	6.59	23.28
Se L	48.67	50.09
Sb L	44.74	26.62
Totals	100.00	

Fig. 2 EDS spectrum of $NaSbSe_2$ nanocrystals with atomic percentages.

~19 nm, which is close to the size determined from the TEM image shown in Fig. 2 below.

The EDS elemental analysis in Fig. 2 displays the percentage of atoms in the $NaSbSe_2$ sample. The ratio of Na : Sb : Se is 1 : 1.14 : 2.15, in close agreement with the atomic ratio 1 : 1 : 2 of $NaSbSe_2$. The residual amount of sulfur in the sample is undetectable, confirming the complete exchange of S with Se.

The TEM images in Fig. 3 show the synthesized particles prior to and after the ion exchange reaction. Fig. 3(a) shows the $NaSbS_2$ NCs and Fig. 3(b) shows the $NaSbSe_2$ NCs deposited on a 30 nm TiO_2 substrate. The $NaSbS_2$ and $NaSbSe_2$ NCs have spherical morphology and exhibit no significant changes in morphology and size after ion exchange. There is no observable aggregation during the SILAR growth of $NaSbSe_2$ NCs. The $NaSbSe_2$ NC size ranges from 15–18 nm, with an average diameter of 17 nm.

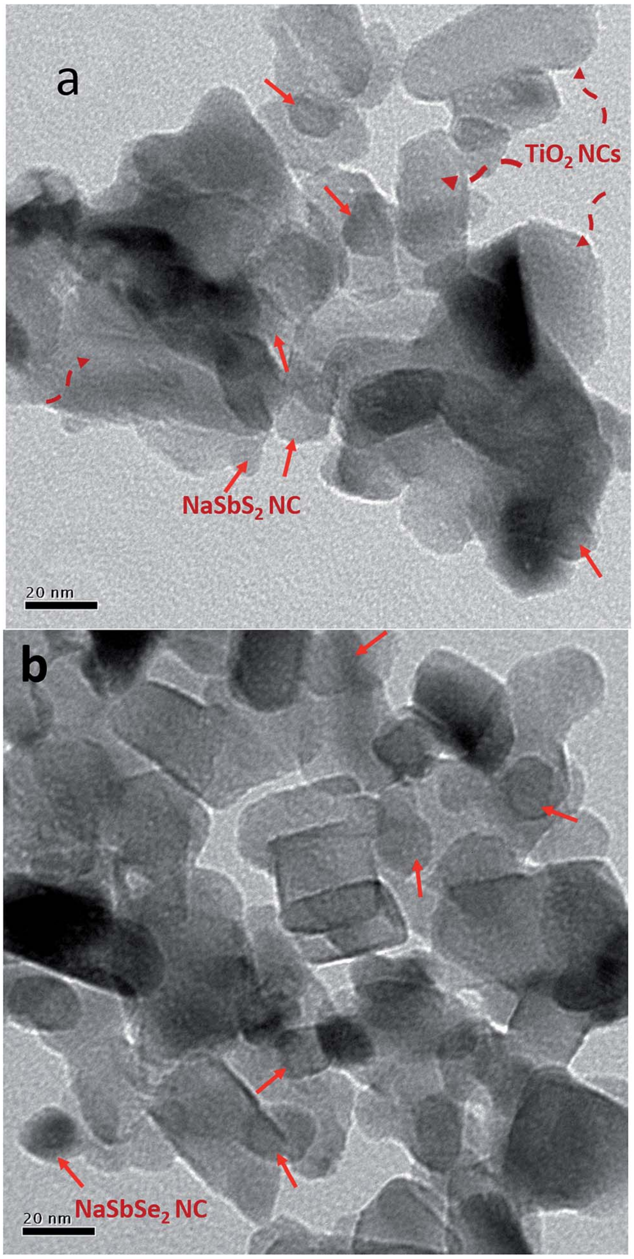

Fig. 3 TEM images of nanocrystals deposited on the surface of TiO_2: (a) $NaSbS_2$ and (b) $NaSbSe_2$. The red solid arrows mark the $NaSbS_2$ or $NaSbSe_2$ NCs while the red-dashed arrows mark TiO_2 particles.

The first principles density of states and direction averaged optical absorption spectra for the ordered monoclinic structure, representing the experiments, and the disordered SQS model are contrasted in Fig. 4. As seen the electronic structure and optical spectrum are very different for these two structures. NaCl structure $NaSbSe_2$ with full cation disorder is found to be semimetallic, with an onset of strong optical absorption at 0.5 eV. The ordered monoclinic structure has a calculated indirect band gap of 0.85 eV. The onset of direct optical absorption is at ~1 eV with strong absorption above ~1.5 eV, roughly in accord with the experimental data. Projections of the density of states (not shown) show substantial hybridization between the Se p orbitals making up the valence bands and the nominally unoccupied Sb p orbitals, similar to $NaSbS_2$. This type of hybridization favors high mobility due to defect screening, as was discussed previously for $NaSbS_2$.[27]

Fig. 5(a) shows the UV-visible transmission spectra $T(\lambda)$ of three Na–Sb–Se samples: $NaSbS_2$, $NaSb(S/Se)_2$ and $NaSbSe_2$. The three samples were prepared with different ion exchange times of 0, 15 and 40 min, respectively, which changed the crystallographic structures from $NaSbS_2$ (0 min) to $NaSb(S/Se)_2$ (15 min) to $NaSbSe_2$ (40 min). The transmission edge of $NaSbS_2$ appears

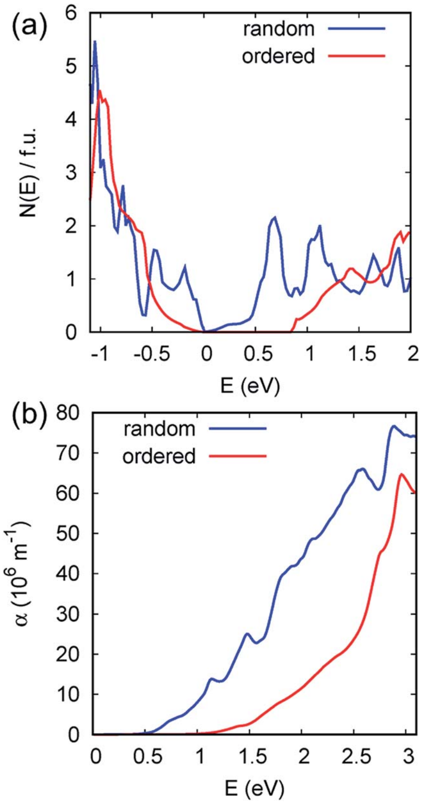

Fig. 4 Calculated electronic density of states (left) and optical absorption (right) for cation disordered and ordered monoclinic $NaSbSe_2$ as obtained with the mBJ potential. No Drude contribution for semimetallic disordered $NaSbSe_2$ is included.

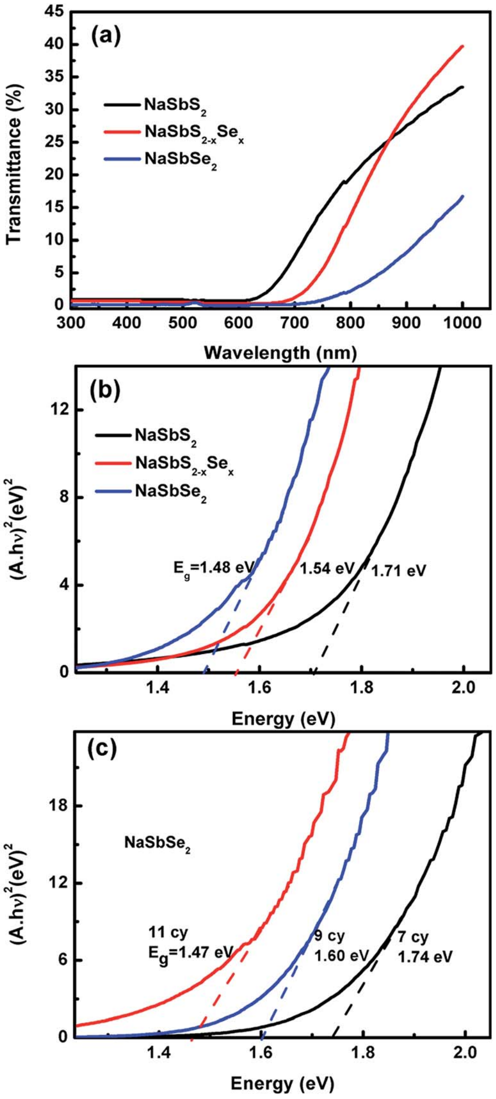

Fig. 5 Optical spectra for NaSbS$_2$, NaSbS$_{2-x}$Se$_x$ and NaSbSe$_2$ NCs: (a) transmission and (b) $(Ah\nu)^2$ *vs.* $h\nu$ plots. (c) E_g of NaSbSe$_2$ NCs prepared with different SILAR cycles.

at a higher energy relative to that of the NaSb(S/Se)$_2$ and NaSbSe$_2$ NCs (see Fig. 5(a)). After 15 minutes of S^{2-} ion exchange reaction with Se^{2-}, a significant redshift in transmission edge was observed. A further red shift in transmission edge was observed after 40 minutes of ion exchange. The transmission edge of NaSbSe$_2$ (determined as the wavelength where $T(\lambda) < 1\%$, *i.e.* absorption = 99%) is ~757 nm, while for NaSbS$_2$ is at a lower wavelength of 630 nm, showing that NaSbSe$_2$ has a broader absorption range. The energy gaps E_g for NaSbS$_2$, NaSb(S/Se)$_2$ and NaSbSe$_2$ NCs were determined from Tauc plots by extrapolating the curves to $y = 0$ as shown in Fig. 5(b). E_g decreases in the order of NaSbS$_2$ (1.71 eV), NaSb(S/Se)$_2$ (1.54 eV), NaSbSe$_2$ (1.48 eV), in agreement with previous reports.[23,24] NaSbSe$_2$ NCs (1.48 eV) have the lowest E_g, resulting in a broader optical absorption range of solar spectrum. The E_g also exhibits a dependence on the particle size of NaSbSe$_2$ NCs. Fig. 5(c) shows the Tauc plots of three NaSbSe$_2$ NCs with different SILAR numbers. The three samples had undergone thorough ion exchange reactions and exhibited the pure NaSbSe$_2$ phase. A lower SILAR number produces smaller-sized NaSbSe$_2$ NCs with a higher E_g due to the quantum size effect.[35] When the SILAR number is increased from 9, 10 to 11, the size of the NaSbSe$_2$ NCs would grow larger and the E_g is lowered from 1.74, 1.60 to 1.47 eV, respectively. A notable feature is that the NaSbSe$_2$ sample with 11 SILAR cycles has an optical E_g of 1.48 eV, which is very close to the optimal E_g of ~1.4 eV for a solar absorber,[36] suggesting that NaSbSe$_2$ has the potential to be a highly efficient solar absorber.

3.1 Photovoltaic performance

Fig. 6 shows the *I–V* curves of NaSbSe$_2$ QDSSCs for various SILAR cycles *n* and counter electrodes under 1 sun illumination. The electrolyte used was polysulfide and the counter electrode was Pt. The photovoltaic parameters – short-circuit current density (J_{sc}), fill factor (FF), open-circuit voltage (V_{oc}) and power conversion efficiency (η) are given in Table 1. The SILAR cycles *n* has a vital effect on the η of the cells. The η of the NaSbSe$_2$ cells increased when *n* was increased from 10 to 11 and then decreased when *n* was further increased to 12 cycles (see Fig. 6 and Table 1, sample nos. 1–3). Therefore the optimum SILAR cycle for NaSbSe$_2$ QDSSCs is $n = 11$. Surface defects are common problems in SILAR-grown NCs. They act as recombination centers for photogenerated charge carriers. Surface

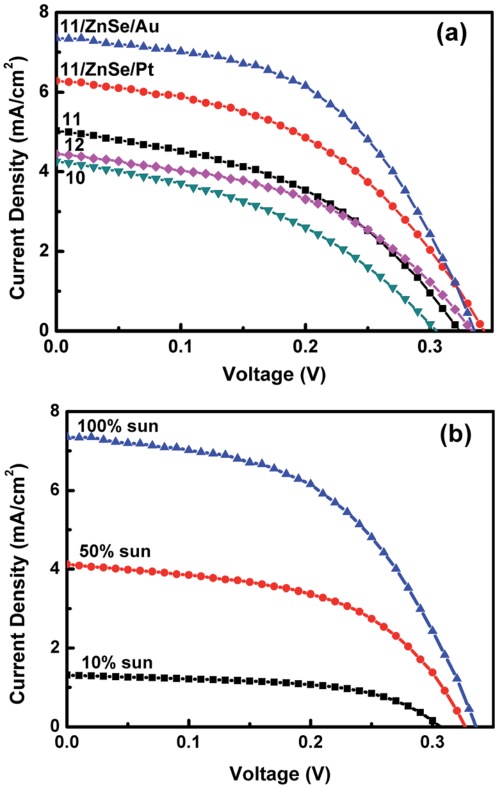

Fig. 6 *J–V* curves of NaSbSe$_2$ QDSSCs: (a) with different SILAR cycles and CEs and (b) under various reduced light intensities. CE: Au; electrolyte: polysulfide.

Table 1 $NaSbSe_2$ QDSSC photovoltaic parameters. Counter electrode (CE): Pt or Au; electrolyte: polysulfide

No	Sample	SILAR cycles n	CE	J_{sc} (mA cm^{-2})	V_{oc} (V)	FF (%)	η (%)
1	$NaSbSe_2$	10	Pt	3.79	0.33	46.1	0.58
2	$NaSbSe_2$	11	Pt	5.03	0.32	43.9	0.71
3	$NaSbSe_2$	12	Pt	4.25	0.30	41.0	0.52
4	$NaSbSe_2$/ZnSe	11	Pt	6.28	0.34	46.1	0.98
5	$NaSbSe_2$/ZnSe	11	Au	7.35	0.33	51.7	1.25

passivation by a layer of ZnS or ZnSe coating could reduce the density of these defect sites.[37] The higher conduction band of ZnSe relative to the conduction band of $NaSbSe_2$ and TiO_2 acts as an energy barrier and prevents the recombination between the photoelectrons in a NC and holes in the polysulfide electrolyte. The efficiency of $NaSbSe_2$ QDSSCs with ZnSe passivation improved from 0.71% (before) to 0.98% (after) (see Fig. 5(a) and Table 1, sample no. 4), an increase of 38%. The efficiency improvement is the result of combined contributions from enhanced J_{sc}, FF and V_{oc}. The effect of counter electrodes (CEs) on the performance of the $NaSbSe_2$ cells was analyzed by employing two types of CEs – Pt and Au. The cell with Au CE exhibited a higher η of 1.25% (sample no. 5), a 27% enhancement relative to Pt CE (0.98%). This is mainly a result of improved J_{sc} = 7.35 mA cm^{-2} and FF = 51.7% with Au CE relative to Pt CE (J_{sc} = 6.28 mA cm^{-2} and FF = 46.1). In a polysulfide electrolyte, a Pt CE has lower electrocatalytic activity relative to an Au CE towards reduction of the electrolyte. This is due to sulfide poisoning of the catalytic active sites of a Pt CE.[38]

Fig. 6(b) displays the I–V curves of $NaSbSe_2$ QDSSCs with Au CE under various reduced light intensities. Table 2 presents the corresponding solar cell parameters. The η increased to 2.22% as the intensity was reduced to 10% sun, a 78% increase over the 1.25% under 1 sun. Moreover, the normalized J_{sc} increased to 13.1 mA cm^{-2}, which is significantly larger than J_{sc} = 7.35 mA cm^{-2} under 1 sun. The improvement in the photovoltaic performance – J_{sc}, FF and η – under reduced light intensities is attributed to a reduced photoelectron–hole recombination rate. The electron–hole (e–h) recombination rate is proportional to the number of e–h pairs generated by the incident light. Under a low light intensity, the absorber generates fewer charge carriers, leading to reduced recombination and improved J_{sc}, FF and η. The significantly improved η under low light intensities indicates that carrier recombination is an active process in the $NaSbSe_2$ QDSSCs.

The efficiency (2.22%) of the present $NaSbSe_2$ cells is lower than that (3.18%) observed in $NaSbS_2$ cells.[23] The different efficiencies are caused mainly by the different open-circuit voltage V_{oc}s: 0.33 V in $NaSbSe_2$ and 0.45 V in $NaSbS_2$. V_{oc} is proportional to the energy gap E_g. As revealed in the present work, $NaSbSe_2$ has a smaller E_g (~1.45 eV) than that (1.8 eV) of $NaSbS_2$. The smaller E_g in $NaSbSe_2$ leads to a smaller V_{oc} and, hence, a smaller efficiency, as shown in this work. The J_{sc} of $NaSbSe_2$ (7.35 mA cm^{-2}) is smaller than that of $NaSbS_2$ (10.76 mA cm^{-2}). In principle, the smaller E_g in $NaSbSe_2$ should produce a larger J_{sc} than that in $NaSbS_2$ with a larger E_g. The reason for the lower J_{sc} is probably due to the surface defects formed on the surface of $NaSbSe_2$ NCs during the ion-exchange reaction. The higher density of surface defects in $NaSbSe_2$ relative to that in $NaSbS_2$ results in a lower J_{sc}. With improved material growth, the problem of surface defects could be reduced and the J_{sc} in $NaSbSe_2$ should eventually surpass the J_{sc} in $NaSbS_2$.

Table 2 $NaSbSe_2$ QDSSC photovoltaic parameters under various reduced sun intensities. CE: Au; electrolyte: polysulfide. The J_{sc} in brackets represents the photocurrent normalized to one sun

Sun power	J_{sc} (mA cm^{-2})	V_{oc} (V)	FF (%)	η (%)
100%	7.35	0.33	51.7	1.25
50%	4.12 (8.24)	0.32	53.5	1.41
10%	1.31 (13.1)	0.30	56.4	2.22

The EQE spectrum covers the spectral range from 300 to 900 nm with the maximum value of 75% at λ = 550 nm, as plotted in Fig. 7. The energy gap of $NaSbSe_2$, determined from the onset of the EQE curve, is $E_g \sim 1.38$ eV, in close agreement with the value (1.48 eV) determined from optical measurements (Fig. 5). Therefore, we conclude based on the optical and EQE data that the E_g of the material is in the range of ~1.4–1.5 eV. The EQE integrated current density J_{ph}, the total photocurrent that the cell can generate, can be determined from the following equation:

$$J_{ph} = e\int_{300}^{900} \Phi(\lambda)\mathrm{EQE}(\lambda)\mathrm{d}(\lambda)$$

where $\Phi(\lambda)$ is the incident light intensity and e is the elementary charge. The integrated photocurrent plotted in the right axis of Fig. 7 yields a total J_{ph} of 14.5 mA cm^{-2}. This is in close agreement with the normalized J_{sc} = 13.1 mA cm^{-2} from the I–V result (see Table 2).

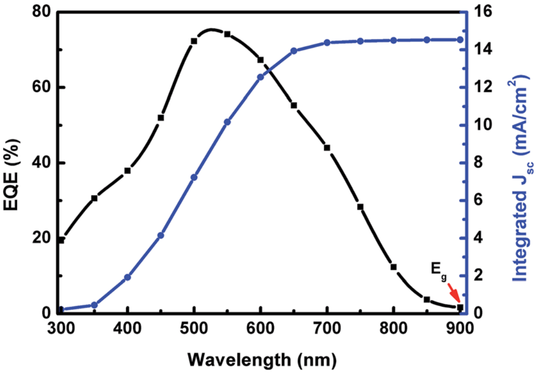

Fig. 7 EQE spectrum.

We summarize the notable results in this work. $NaSbSe_2$ NCs were synthesized from the $NaSbS_2$ precursor using the ion exchange method. The synthesized $NaSbSe_2$ has larger lattice constants as well as a reduced optical E_g (1.48 eV) compared to that of the parent $NaSbS_2$. This E_g is very close to the optimal E_g of a solar absorber. First principles calculations show that the synthesis method is crucial in yielded NCs with cation order and in particular that the cation disorder in material grown at high temperature will be detrimental. The best cell exhibited an efficiency of 2.2% under 0.1 sun, a respectable value for the first report of a new solar material. Since the synthesis method is a general technique, many new ternary metal selenide-based solar materials can be produced following the same technique used in this work.

4. Conclusion

In summary, we have successfully synthesized NCs from the as-synthesized Na–Sb–S precursor by the solution-phase Se^{2-} anion exchange reaction. A reaction time of 40 min completed the $NaSbS_2$ to $NaSbSe_2$ exchange reaction. $NaSbSe_2$ NCs exhibit the same crystal structure as the parent $NaSbS_2$ precursor with larger lattice constants and a lower E_g of 1.48 eV relative to $NaSbS_2$ (1.71 eV). The best solar cell was prepared using 11 SILAR cycles, an Au counter electrode and a ZnSe passivation coating. The best cell exhibits a normalized $J_{sc} = 13.1$ mA cm^{-2}, a $V_{oc} = 0.30$ V, a FF = 56.4% and an $\eta = 2.22\%$. The near-optimal E_g suggests that $NaSbSe_2$ has the potential to be a highly efficient solar material.

Conflicts of interest

There is no conflict to declare.

Acknowledgements

The authors are grateful to the financial support from the Ministry of Science and Technology of the Republic of China under grant Nos. MOST 103-2112-M-005-004-MY3 and MOST 105-2811-M-005-008. Work at the University of Missouri was supported by the U.S. Department of Energy through the S3TEC Energy Frontier Research Center, Award Number DE-SC0001299/DEFG02-09ER46577.

References

1 P. V. Kamat, *J. Phys. Chem. C*, 2008, **112**, 18737–18753.
2 J. Tian and G. Cao, *J. Phys. Chem. Lett.*, 2015, **6**, 1859–1869.
3 V. González-Pedro, X. Xu, I. Mora-Seró and J. Bisquert, *ACS Nano*, 2010, **4**, 5783–5790.
4 J. Tian, T. Shen, X. Liu, C. Fei, L. Lv and G. Cao, *Sci. Rep.*, 2016, **6**, 23094.
5 R. J. Ellingson, M. C. Beard, J. C. Johnson, P. Yu, O. I. Micic, A. J. Nozik, A. Shabaev and A. L. Efros, *Nano Lett.*, 2005, **5**, 865–871.
6 M. Green, in *Third Generation Photovoltaics: Advanced Solar Energy Conversion*, Springer Berlin Heidelberg, Berlin, Heidelberg, 2003, DOI: 10.1007/3-540-26563-5_3, pp. 21–34.
7 S. N. Guin, A. Chatterjee, D. S. Negi, R. Datta and K. Biswas, *Energy Environ. Sci.*, 2013, **6**, 2603–2608.
8 S. N. Guin, V. Srihari and K. Biswas, *J. Mater. Chem. A*, 2015, **3**, 648–655.
9 S. N. Guin and K. Biswas, *Chem. Mater.*, 2013, **25**, 3225–3231.
10 C. Xiao, X. Qin, J. Zhang, R. An, J. Xu, K. Li, B. Cao, J. Yang, B. Ye and Y. Xie, *J. Am. Chem. Soc.*, 2012, **134**, 18460–18466.
11 C.-L. Chou, N. Suriyawong, B. Aragaw, J.-B. Shi and M.-W. Lee, *J. Electrochem. Soc.*, 2016, **163**, H445–H449.
12 N. Liang, W. Chen, F. Dai, X. Wu, W. Zhang, Z. Li, J. Shen, S. Huang, Q. He, J. Zai, N. Fang and X. Qian, *CrystEngComm*, 2015, **17**, 1902–1905.
13 Z. Liu, J. Huang, J. Han, T. Hong, J. Zhang and Z. Liu, *Phys. Chem. Chem. Phys.*, 2016, **18**, 16615–16620.
14 M. Bernechea, N. C. Miller, G. Xercavins, D. So, A. Stavrinadis and G. Konstantatos, *Nat. Photonics*, 2016, **10**, 521–525.
15 N. Suriyawong, B. Aragaw, J.-B. Shi and M.-W. Lee, *J. Colloid Interface Sci.*, 2016, **473**, 60–65.
16 P.-C. Huang, W.-C. Yang and M.-W. Lee, *J. Phys. Chem. C*, 2013, **117**, 18308–18314.
17 M. Kumar and C. Persson, *IRESR*, 2013, vol. 5, p. 031616.
18 K. Ramasamy, B. Tien, P. S. Archana and A. Gupta, *Mater. Lett.*, 2014, **124**, 227–230.
19 S. Dekhil, H. Dahman, S. Rabaoui, N. Yaacoub and L. El Mir, *J. Mater. Sci.: Mater. Electron.*, 2017, **28**, 11631–11635.
20 L. Wang, C. Ma, K. Hu, R. Zhou, X. Mao, S. Pan, L. H. Wong and J. Xu, *J. Alloys Compd.*, 2016, **680**, 182–190.
21 W. Septina, S. Ikeda, Y. Iga, T. Harada and M. Matsumura, *Thin Solid Films*, 2014, **550**, 700–704.
22 W.-C. Yang and M.-W. Lee, *J. Electrochem. Soc.*, 2014, **161**, H92–H96.
23 S. U. Rahayu, C.-L. Chou, N. Suriyawong, B. A. Aragaw, J.-B. Shi and M.-W. Lee, *APL Mater.*, 2016, **4**, 116103.
24 V. A. Bazakutsa, N. I. Gnidash, A. K. Kul'chitskaya and A. V. Salov, *Phys. Usp.*, 1975, **18**, 472–475.
25 M. D. Nielsen, V. Ozolins and J. P. Heremans, *Energy Environ. Sci.*, 2013, **6**, 570–578.
26 S. I. Berul', Y. G. Finkel'shtein and N. P. Luzhnaya, in *Chemical Bonds in Solids: Semiconductor Crystals, Glasses, and Liquids*, ed. A. N. N. Sirota, Springer US, Boston, MA, 1995, vol. 4, DOI: 10.1007/978-1-4684-8682-7_28, pp. 149–154.
27 J. Sun and D. J. Singh, *Phys. Rev. Appl.*, 2017, **7**, 024015.
28 F. Huang, J. Hou, Q. Zhang, Y. Wang, R. C. Massé, S. Peng, H. Wang, J. Liu and G. Cao, *Nano Energy*, 2016, **26**, 114–122.
29 S. H. Wei and A. Zunger, Disorder Effects on the Density of States of the II-VI Semiconductor Alloys $Hg_{0.5}Cd_{0.5}Te$, $Cd_{0.5}Zn_{0.5}Te$ and $Hg_{0.5}Zn_{0.5}Te$, *Phys. Rev. B: Condens. Matter Mater. Phys.*, 1991, **43**, 14272.
30 J. P. Perdew, K. Burke and M. Ernzerhof, Generalized Gradient Approximation Made Simple, *Phys. Rev. Lett.*, 1996, **77**, 3865.

31 G. Kresse and D. Joubert, From Ultrasoft Pseudopotentials to the Projector Augmented-Wave Method, *Phys. Rev. B: Condens. Matter Mater. Phys.*, 1999, **59**, 1758.

32 F. Tran and P. Blaha, Accurate Band Gaps of Semiconductors and Insulators with a Semilocal Exchange–Correlation Potential, *Phys. Rev. Lett.*, 2009, **102**, 226401.

33 D. J. Singh, Electronic Structure Calculations with the Tran-Blaha Modified Becke-Johnson Density Functional, *Phys. Rev. B: Condens. Matter Mater. Phys.*, 2010, **82**, 205102.

34 C. A. Jacobson, E. C. Weaver and C. A. Hampel, *Encyclopedia of chemical reactions*, Reinhold Pub. Corp., New York, 1946.

35 S. Gorer and G. Hodes, *J. Phys. Chem.*, 1994, **98**, 5338–5346.

36 T. Zdanowicz, T. Rodziewicz and M. Zabkowska-Waclawek, *Sol. Energy Mater. Sol. Cells*, 2005, **87**, 757–769.

37 F. Huang, Q. Zhang, B. Xu, J. Hou, Y. Wang, R. C. Masse, S. Peng, J. Liu and G. Cao, *J. Mater. Chem. A*, 2016, **4**, 14773–14780.

38 G. Hodes, J. Manassen and D. Cahen, *J. Electrochem. Soc.*, 1980, **127**, 544–549.